Chemical Engineering Journal 472 (2023) 144872

Contents lists available at ScienceDirect

Chemical Engineering Journal

journal homepage: www.elsevier.com/locate/cej

# Oriented self-assembly of anisotropic layered double hydroxides (LDHs) with 2D-on-3D hierarchical structure

Jingjing Cao [a], Zimou Feng [a], Huaxing Liang [a], Xinglin Lu [a,1,*], Wei Wang [b,c,1,*]

[a] CAS Key Laboratory of Urban Pollutant Conversion, Department of Environmental Science and Engineering, National Synchrotron Radiation Laboratory, University of Science and Technology of China, Hefei 230026, China
[b] Department of Chemistry, University of Bergen, Bergen, 5007, Norway
[c] Centre for Pharmacy, University of Bergen, Bergen, 5020, Norway

ARTICLE INFO

*Keywords:*
Anisotropic 2D-on-3D LDHs
Oriented self-assembly
Oriented attachment
Ostwald ripening
Energy storage

ABSTRACT

Layered double hydroxides (LDHs) have been the subject of increasing research due to their unique 2D or 3D structures and promising applications. However, achieving precise control over their morphology and architecture has proven to be a significant challenge. In this work, we present an oriented self-assembly strategy for the synthesis of ultrathin 2D-on-3D CoNi-LDHs nanoflowers (NFs) at ambient temperature. *Ex situ* and *in situ* characterization techniques were employed to elucidate the formation process of the 2D-on-3D CoNi-LDHs hierarchical structure. The 2D nanosheets are composed of $CoNi(OH)_2$ seeds that undergo rapid nucleation and growth. Under the influence of oriented attachment and Ostwald ripening, the 2D nanosheets continue to crystallize along the axial and radial directions, resulting in the formation of 2D-on-3D CoNi-LDH NFs. This unique 2D-on-3D LDHs structure possesses an ultrathin thickness of approximately 1.5 nm, nanopores with a diameter of approximately 3.8 nm, and a large surface area of approximately 154 $m^2/g$. These properties manifest excellent energy-storage performance in supercapacitors. Our approach provides important insights into the precise synthesis of LDHs with a 2D-on-3D hierarchical structure. The synthesis of LDHs with well-defined structures is a significant challenge in materials science. Our work contributes to the advancement of this field and has the potential to facilitate the development of new, high-performance energy-storage devices.

## 1. Introduction

Layered double hydroxides (LDHs) represent a class of 2D nanomaterials, which possess a chemical structure akin to $[M^{2+}_{1-x}M^{3+}_{x}(OH)_2]^{x+}$ $[A^{n-}_{x/n}\cdot mH_2O]$, where $M^{2+}/M^{3+}$ and $A^{n-}$ denote divalent/trivalent metal ions and charge-balancing anions, respectively [1–3]. These materials are commonly synthesized in either aqueous or organic solvents, where reaction additives such as alkali sources, surfactants, and salt ions, along with precise temperature control, resulting in a convective reaction solution that reaches a supersaturated state, thus prompting crystal precipitation and growth [4]. The LDHs formed under such hydrothermal/solvothermal conditions [5–7] exhibit two primary structures, including two-dimensional (nanosheets and nanoribbons) [8] and three-dimensional (nanoflowers) materials [9,10]. By finetuning the microstructures of LDHs (such as crystal and electronic structures) and designing their macrostructures on the morphological scale [11], LDHs display remarkable catalytic and electrochemical performance [12]. These exceptional properties hold vast potential for myriad applications, such as water splitting/oxidation [13–15], photocatalysis [16–17], oxygen/hydrogen evolution, [18–21], and supercapacitors [22–24].

In the liquid phase, well-dispersed two-dimensional (2D) LDHs exhibit a high specific surface area and abundant active sites, which facilitate the diffusion of ions/molecules and the transfer of electrons. However, previous investigations have demonstrated that the thickness of the acquired LDHs is largely greater than 10 nm, indicating the stacking of multiple nanosheets. This stacking hinders the exposure of LDH surfaces between adjacent nanosheets, thereby lowering catalytic performance and long-term stability. Recent studies have endeavored to construct three-dimensional (3D) LDHs with structures that can further enhance catalytic/electrochemical performance and augment stability [25–26]. These 3D LDHs are formed on a substrate (such as carbon cloth,

* Corresponding authors.
*E-mail addresses:* xinglinlu@ustc.edu.cn (X. Lu), wei.wang@uib.no (W. Wang).
[1] These authors jointly supervised this work.

https://doi.org/10.1016/j.cej.2023.144872
Received 5 May 2023; Received in revised form 11 July 2023; Accepted 16 July 2023
Available online 18 July 2023

metal mesh, or graphene) [27–31] *via* laboratory-scale procedures (with a volume less than 50 mL) [4,32,33]. However, given that the synthesis reactions require stringent conditions like high temperature and pressure, it proves challenging to scale up the existing procedures for producing large amounts of LDHs that are fit for real-world applications.

During synthesis, the nascent LDHs exist predominantly in the form of a block or thick matrix [34]. This phenomenon is likely due to various factors that emerge during the synthesis process. Firstly, divalent/trivalent metal salts have a tendency to hydrolyze under alkaline conditions, which can lead to their aggregation into solid nanoparticles before co-assembly occurs [35]. Secondly, while the LDH structure is driven by the controllable assembly of nanoparticles between surfactants or structural guides under hydrothermal conditions, the resulting structures of LDHs are largely uncontrollable [36,37]. Therefore, the synthesis of ultrathin 2D nanosheets on 3D architectures is deemed a promising strategy for LDH applications. Such a 2D-on-3D hierarchy structure incorporates the benefits of both types of LDHs, such as high exposure of ultrathin 2D nanosheets and great stability of the 3D structure, for the aforementioned applications [38–40]. More importantly, the growth of 2D nanosheets into 3D structures is likely to result in channels with varying directions, thereby enhancing ion/molecule diffusion and increasing absorption capacity [41–43]. Nevertheless, the orderly synthesis of a 2D-on-3D hierarchy structure in a controlled manner is by far difficult, primarily due to the absence of a self-assembly system capable of generating 2D ultrathin nanosheets and 3D scaffold architectures concurrently.

In this work, we present an oriented self-assembly strategy that has been developed to synthesize ultrathin cobalt–nickel nanoflowers (2D-on-3D CoNi-LDH NFs) under ambient conditions. The introduction of ethanolamine into an ethanol/water system generates an alkaline environment that facilitates nucleation and oriented self-assembly at the interface. The resulting ultrathin 2D-on-3D CoNi-LDH NFs have been extensively characterized in order to elucidate their formation mechanisms and evaluate their electrochemical performance. Our results indicate that the synthesis reaction underwent oriented attachment and Ostwald ripening processes, which regulated the growth of nanocrystalline seeds in an oriented manner, leading to the crystallization of ultrathin 2D-on-3D CoNi-LDH NFs. These nanoflowers exhibit a large surface area of approximately 154 $m^2/g$, an ultrathin nature of single nanosheets (~1.5 nm), and an anisotropic 3D structure. Furthermore, the synthesized 2D-on-3D CoNi-LDH NFs exhibit a superior capacity of 371 mAh/g (2400F/g at 1 A/g), which results in a high voltage of 1.7 V, an energy density of 98.9 Wh $kg^{-1}$ at an ultrahigh power density of 17981 W $kg^{-1}$. These properties make them highly advantageous for supercapacitor applications. It is worth noting that the anode made from this material also displays excellent cycle stability, indicating its great potential for a range of real-world electrochemical applications.

## 2. Results and discussion

**Synthesis and characterization of 2D-on-3D CoNi-LDH NFs.** In the usual method of producing CoNi NSs (as shown in Scheme 1A), NaOH is used as a precipitant, causing the accumulation and expansion of seeds to form bulk cobalt–nickel LDH (bulk CoNi-LDH). Our approach, however, involves synthesizing 2D-on-3D CoNi-LDHs NFs at room temperature using a combination of self-assembly techniques known as an oriented attachment and Ostwald ripening growth (Scheme 1B). In our synthesis design, we used cobalt chloride hexahydrate and nickel chloride hexahydrate as metal precursors, with ethanolamine serving as a structure-directing agent and base source. The solvent used for hydrolyzing ethanolamine was a mixture of ethanol and water. $NH_3^+(CH_2)_2OH$ was released as a complexing agent to regulate the formation and growth orientation of the seeds. The synthesis process begins at the interface between ethanolamine and the ethanol/water mixture, where $NH_3^+(CH_2)_2OH$, $OH^-$, $Co^{2+}$, and $Ni^{2+}$ combine to form nanocrystalline seeds through oriented attachment, leading to the creation of 2D CoNi NSs. Subsequently, anisotropic self-assembly occurs, resulting in the formation of 2D-on-3D CoNi-LDHs NFs.

We used scanning electron microscopy (SEM) and transmission electron microscopy (TEM) to observe the morphology of the products. The bulk CoNi-LDHs (Fig. 1B and 1F) show a disorderly arrangement. Conversely, the 2D-on-3D CoNi-LDHs NFs display a 3D flower-shaped anisotropic architecture (Fig. 1A and 1E) that consists of ultrathin 2D NSs with a uniform size distribution. Energy dispersive spectroscopy (EDS) confirms that cobalt, nickel, and oxygen are evenly distributed in both the 2D-on-3D CoNi-LDHs NFs (Fig. 1C) and the bulk CoNi-LDHs (Fig. 1D). We used atomic force microscopy (AFM) to measure the thickness of the 2D-on-3D CoNi-LDHs NFs, which is approximately 1.5 nm. This indicates a structure composed of three layers of CoNi LDH with an ultrathin 2D structure (Fig. 1G). In contrast, the bulk CoNi-LDHs have a thickness of about 20 nm (Fig. S1), suggesting the presence of multiple layers stacked together.

High-resolution TEM (HRTEM) was employed to examine the microscopic crystal structure of the materials. The 2D-on-3D CoNi-LDHs NFs revealed the presence of nanopores measuring 2–4 nm (white circles in Fig. 1H and Fig. S2B). These nanopores were not found in the bulk CoNi-LDHs (Fig. 1I and Fig. S2A). Interestingly, the nanopores in the 2D-on-3D CoNi-LDHs NFs seemed to be roughly spherical, which could have been generated *via* Ostwald ripping that preferentially consumes the prominent atoms. Furthermore, the crystal fringe spacing of the 2D-on-3D CoNi-LDHs NFs and bulk CoNi-LDHs exposed crystal faces is 2.6 Å and 2.3 Å, respectively, corresponding to the plane spacing of (0 1 2) and (0 1 5). The presence of nanopores in 2D-on-3D CoNi-LDHs NFs likely increases the oxygen vacancy density and the number of free electrons in the CoNi center, resulting in an extremely strong EPR signal of the sample, as exhibited in Fig. 1J. In contrast, the weak EPR strength of bulk CoNi-LDHs without nanopores is attributed to the formation of CoNi-saturated coordination species and dipolar interactions between CoNi ions, which significantly reduce the availability of free electrons.

Nitrogen adsorption–desorption isotherms have been used to determine the surface area and pore size distribution of the samples. The 2D-on-3D CoNi-LDHs NFs show a specific surface area of 154 $m^2/g$, which is 3.14 times larger than that of the bulk CoNi LDH. The pore size distribution curves, based on the $N_2$ desorption data (Fig. S3 and Table S1), confirm the presence of pores with a diameter of 3.8 nm, consistent with the HRTEM analysis results. The pore volume calculated from the $N_2$

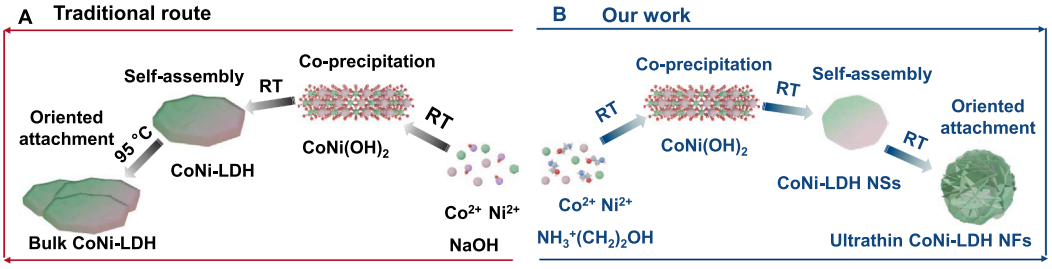


**Scheme 1. A, B** Illustration of synthesis procedure of the bulk CoNi LDH (traditional route) and 2D-on-3D CoNi-LDH NFs (our work).

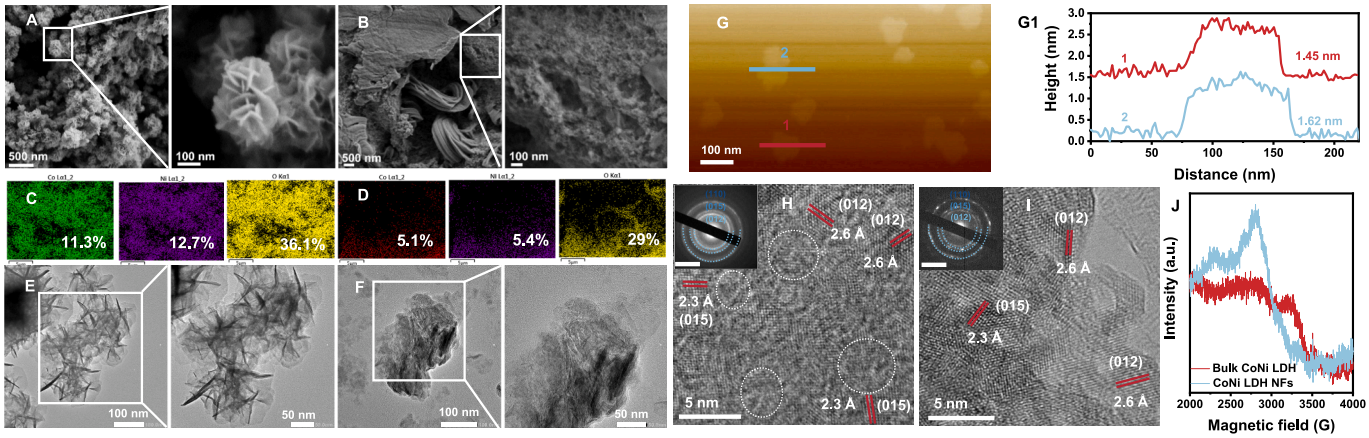


**Fig. 1.** Structural characteristics of the 2D-on-3D CoNi-LDH NFs and bulk CoNi LDH. **A, B** SEM images, **C, D** EDS images, **E** ~ **F** TEM images, **G** AFM images, **H, I** HRTEM images, and **J** EPR spectra.

desorption branch, known as Barrett-Joyner-Halenda (BJH), demonstrates that the 2D-on-3D CoNi-LDHs NFs have a significantly higher pore volume (0.643 $cm^3\ g^{-1}$) compared to bulk CoNi-LDHs (0.086 $cm^3\ g^{-1}$), confirming the high porosity of the 2D-on-3D CoNi-LDHs NFs. Overall, the anisotropic architecture of 2D-on-3D CoNi-LDHs NFs possesses ultrathin and nanoporous characteristics that enhance mass transport within the material.

The application of X-ray diffraction (XRD) techniques to the analysis of bulk CoNi-LDHs and 2D-on-3D CoNi-LDHs NFs (Fig. 2A) has revealed an assortment of distinct diffraction peaks, precisely located at 2θ values of 11.9°, 22.8°, 34.3°, 34.8°, 38.7°, 45.7°, 60.9°, 61.4°, and 71.3°. These peaks can be unequivocally attributed to the crystallographic planes denoted by their corresponding Miller indices, namely (003), (006), (101), (012), (015), (018), (110), (113), and (112), respectively. These patterns of diffraction precisely match the standard pattern of CoNi-LDHs (JCPDS 33-0429) and α-$Ni(OH)_2$ (JCPDS 38-0715). In addition, the XRD patterns obtained from bulk CoNi-LDHs prove to be harmonious with the anticipated diffraction behavior of CoNi-LDHs (JCPDS 33-0429). Furthermore, analogous patterns of diffraction observed for cobalt/nickel metal ratios also exhibit compelling compatibility with α-$Ni(OH)_2$ (JCPDS 38-0715) (Fig. S4).

Additionally, X-ray photoelectron spectroscopy (XPS) was employed to reveal the electronic states of the materials. The Co *2p* spectrum of 2D-on-3D CoNi-LDHs NFs (Fig. 2C) exhibited binding energies at 797.3 and 781.7 eV, which corresponded to the Co $2p_{1/2}$ signal peaks of $Co^{2+}$ and Co $2p_{1/2}$ signal peaks of $Co^{3+}$. These signals indicated the presence of the

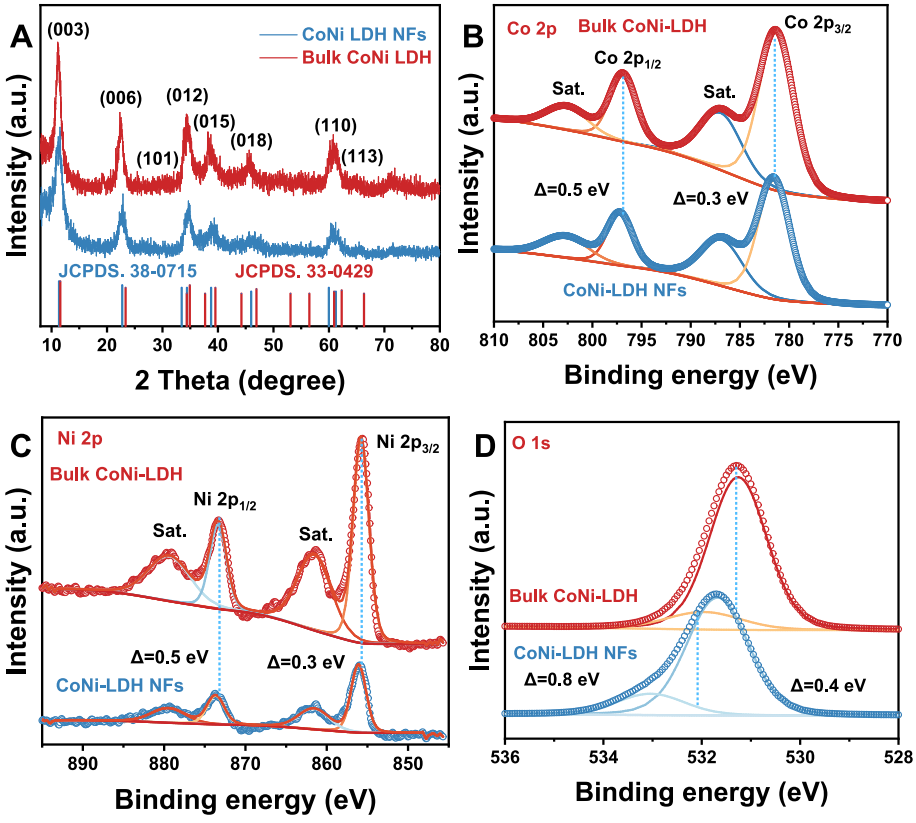


**Fig. 2.** Comparison of crystalline structure and composition of 2D-on-3D CoNi-LDH NFs and bulk CoNi LDH. **A** The XRD patterns of 2D-on-3D CoNi-LDH NFs and bulk CoNi LDH. High-resolution XPS elemental spectra of **B** Co *2p*, **C** Ni *2p*, **D** O *1 s* of 2D-on-3D CoNi-LDH NFs and bulk CoNi LDH.

$Co^{3+}/Co^{2+}$ state in the materials. Moreover, the binding energies at 873.9 and 856.1 eV corresponded to the Ni $2p_{1/2}$ and Ni $2p_{3/2}$ signal peaks of $Ni^{2+}$, implying the valence state of $Ni^{2+}$ (Fig. 2C). Compared to bulk CoNi-LDHs, the Co *2p* and Ni *2p* energy spectra of 2D-on-3D CoNi-LDHs NFs shifted to a higher binding energy by about 0.3 ~ 0.5 eV, indicating electron deficiency of 2D-on-3D CoNi-LDHs NFs. The energy spectrum of O 1 s (Fig. 2D) could be deconvoluted into two peaks at 531.7 eV and 532.9 eV, which corresponded to oxygen in hydroxyl groups (–OH) and adsorbed $H_2O$ molecules, respectively. Compared with bulk CoNi-LDHs, the O 1 s energy spectrum shifted to a higher binding energy, consistent with the results of Co *2p* and Ni *2p* energy spectra.

**Formation mechanisms of 2D-on-3D CoNi-LDHs NFs.** To unravel the mechanisms underlying the formation of ultrathin 2D-on-3D CoNi-LDHs NFs, we meticulously observed the morphology evolution at different time stages (Fig. 3A) and identified a three-step formation process.

Step 1 involves the nucleation and growth stage, which occurs within a mere 30 s. During this stage, $Ni^{2+}$ and $Co^{2+}$ react swiftly with $OH^-$ to form CoNi-OH seeds, which quickly aggregate into primary CoNi-OH nanocrystals (Fig. 3B). $NH_3^+(CH_2)_2OH$ tends to adsorb on the (1 1 0) facets of CoNi-OH nanocrystals, facilitated by electrostatic interactions and hydrogen bonding among $NH_3^+(CH_2)_2OH$, $Ni^{2+}$, and $Co^{2+}$. This drives the formation of nanocrystals through an oriented attachment process, taking advantage of the large specific surface area and high specific surface energy of the nanocrystals, which increases the total energy of the system. This energy increase leads to the oriented attachment of nanocrystals along the crystal plane with higher energy. After 5–10 s, the crystal axes along the axis (0 0 1) and the radial axis (1 0 1) were oriented, forming 2D nanosheets with slightly larger folds (Fig. 3C and 3D).

To investigate the nanocrystal formation process at the initial stage of the reaction, *in situ* SAXS was employed (Fig. 3L). The scattering vector, q, ranges from 0.08 to 4 $nm^{-1}$, corresponding to the spatial size of 1.6 – 78.5 nm. Within the first second of the reaction, CoNi-OH nanocrystalline self-assembly and aggregation occurred, and the size was beyond the detection range of SAXS (>78.5 nm). These results indicate that a high-energy system formed at the initial stage of the reaction, which accelerated the completion of the self-assembly of the reaction system.

After 30 s of reaction time, the folded nanosheets formed an initial scale of 2D folded nanosheets by means of anisotropic attachment (Fig. 3E). The (1 1 0) facet of the $CoNi(OH)_2$ seeds is more stable than the (0 1 2) and (0 1 5) facets with high surface energy (Fig. 3J and S5-7), which renders the (1 1 0) facet more attractive to $NH_3^+(CH_2)_2OH$ adsorption to further reduce surface energy. This results in the (1 1 0) facet of the $CoNi(OH)_2$ seeds possessing a positive charge, which drives the organization of small seeds into nanosheets through an oriented attachment process facilitated by electrostatic interactions and hydrogen-bond interactions between the $NH_3^+(CH_2)_2OH$ adsorbents. Ethanolamine plays a vital role in initial orientation, nucleation, and growth in this step. It can promote the formation of CoNi-OH-$[NH_3^+(CH_2)_2OH]$ in an aqueous solution, regulate the release of cobalt/nickel ions from the complex, and ultimately affect the precipitation rate of CoNi-OH.

Step 2: the oriented attachment process. As the reaction progresses for 1 min, the self-assembly of 2D wrinkle nanosheets exhibited an orientational disposition, yielding a remarkable 3D nanoflower structure (Fig. 3F). Upon extending the reaction time to 5 min, the 2D ultrathin nanosheets of the architecture witness a further increase in both their lateral size and dimensions. It is during this progression that small crystal nuclei agglomerate to form large particles, while the 2D ultrathin nanosheets experience pronounced wrinkling (Fig. 3G and 3 K). The outcome of this process is a 3D nanoflower arrangement, comprising nanosheets characterized by 2D approximate hexagonal and wrinkling surfaces. After a span of 30 min, the size of the material undergoes a significant increase, while the phase remains largely unaltered from its initial state (Fig. 3H and 3 M).

Steps 3–4: the process of crystallization whereby ultrathin wrinkle nanosheets transform into ultrathin nanosheets is dominated by the confluence of self-assembly and Ostwald ripening mechanisms. The resulting anisotropic nanosheets are assembled into a 2D-on-3D CoNi-LDHs NFs nanoflower architecture (Fig. 3I). Following a reaction period of 6 h, the ultrathin nanosheets continue to crystallize in both axial and radial directions, continuing in the formation of flower-like 2D-on-3D CoNi-LDHs NFs with high crystallinity and stability. The thickness of the nanocrystals is uniform in both axial and radial directions, giving rise to a complete and uniform crystal surface. The

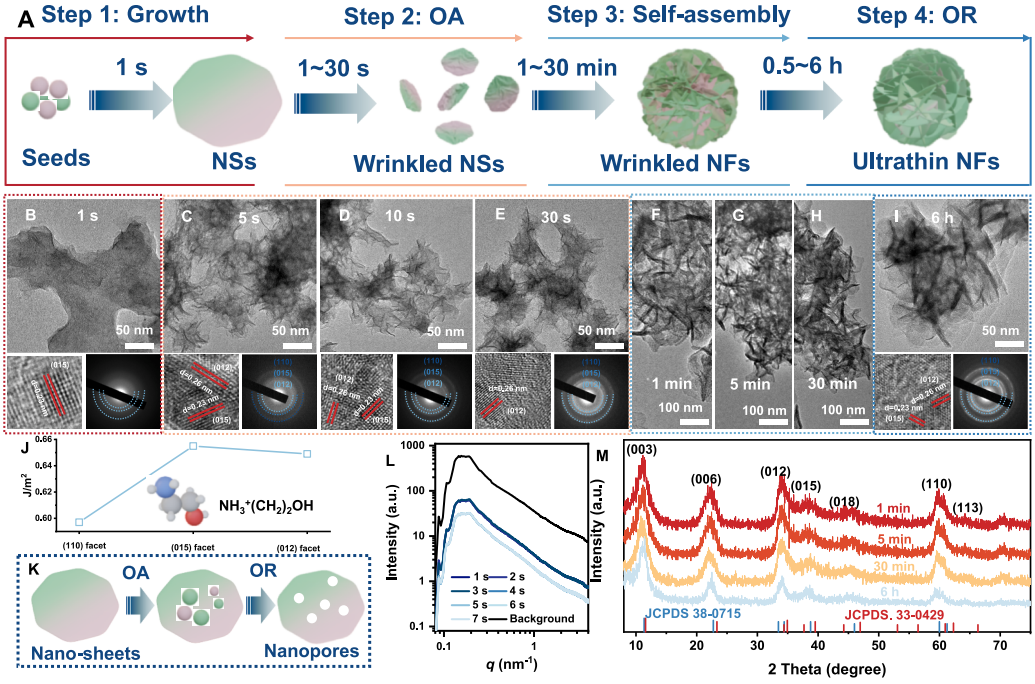


**Fig. 3.** The formation mechanisms of 2D-on-3D CoNi-LDH NFs. **A** Schematic illustration for 2D-on-3D CoNi-LDH NFs morphology evolution. **B** ~ **I** TEM images of the intermediate products at different reaction stages: **B** 1 s, **C** 5 s, **D** 10 s, **E** 30 s, **F** 1 min, **G** 5 min, **H** 30 min, **G** 6 h. **J** Surface energies profiles of the 2D-on-3D CoNi-LDH NFs. **K** Schematic of the oriented attachment (OA) and Ostwald ripening (OR) strategy for the formation of nanosheets to nanopores. **L** *in situ* SAXS spectra of 2D-on-3D CoNi-LDH NFs within 1–7 s. **M** XRD patterns of 2D-on-3D CoNi-LDH NFs at different reaction stages.

nanosheets then merge and grow to form nanoflower. The role of crystal anisotropy in the creation of the CoNi-OH monolayer is noteworthy. Interestingly, during the self-assembly stage, the crystals undergo anisotropic attachment, and the in-layer Ostwald ripening process causes the nanocrystals to shrink further, eventually forming the ultrathin 2D-on-3D nanosheets-nanopores architecture (Fig. 3J and 3 K). It is important to note that the in-layer Ostwald ripening process creates a large amount of evenly distributed nanopores in the ultrathin 2D-on-3D CoNi-LDHs NFs nanopores, leading to a significant increase in ionic accessibility and active sites.

**Electrochemical properties of 2D-on-3D CoNi-LDHs NFs.** The charging and discharging process of the 2D-on-3D CoNi–LDH NFS is a quasi-adsorption/desorption process of hydrogen atoms on the surface, and the architecture with more hydrogen ions exposed is favorable for electrochemical redox reactions. The ultrathin and anisotropic architecture 2D-on-3D CoNi-LDHs NFs facilitates fast charge transport, and $OH^-$ anions readily enter the 2D-on-3D CoNi-LDHs NFs interlayer to form CoOOH or NiOOH complexes. The charging and discharging process reflects the intercalation – deintercalation of $OH^-$ ions in 2D-on-3D CoNi-LDHs NFs. When $Co^{2+}$ and $Ni^{2+}$ ions are oxidized in 2D-on-3D CoNi-LDHs NFs, the average oxidation state increases. To remain electrical neutrality, $OH^-$ anions enter the interlayer. This 2D-on-3D architecture with mesoporous pores and defects provides more active sites for the redox process, promotes ion diffusion, and thus improves the electrochemical performance of the electrode. The energy storage process can be expressed by the equation:

$$NiCo(OH)_2 + 2OH^- \leftrightarrow NiOOH + CoOOH + H_2O + 2e^-$$

$$CoOOH + 2OH^- \leftrightarrow CoO_2 + H_2O + 2e^- \quad (1)$$

The cyclic voltammetry (CV) curves of bulk CoNi-LDHs and 2D-on-3D CoNi-LDHs NFs at a scan rate of 5 mV $s^{-1}$ with a potential window of 0–0.6 V (Fig. 4A). The CV curves of 2D-on-3D CoNi-LDHs NFs electrode exhibit the largest integral area. This phenomenon indicates the high specific capacity of the 2D-on-3D CoNi-LDHs NFs, which may result from the synergistic effect of ultrathin 2D architecture and 3D anisotropic architecture. The discharging time of 2D-on-3D CoNi-LDHs NFs is the longest as shown in the galvanostatic charge–discharge (GCD) curves at 1 A/g (Fig. 4B). With a discharge current density of 1 A/g, the maximum specific capacity of 2D-on-3D CoNi-LDHs NFs (371.9 mAh/g, equivalent to 2400F/g) was almost tripled in value relative to that of bulk CoNi-LDHs (128.1 mAh/g, equivalent to 974F/g). Such performance is much better than those of Co/Ni-based LDH NFs reported in previous studies (largely in the range of 80–350 mAh/g) (data summarized in Figs. S8-S11 and Table S2).

Electrochemical impedance was used to characterize material conductivity (Fig. 4C). The 2D-on-3D CoNi-LDHs NFs electrode is steeper than the bulk CoNi-LDHs electrode in the low-frequency region, indicating low diffusion resistance of the 2D-on-3D CoNi-LDHs NFs electrode. The 2D-on-3D CoNi-LDHs NFs electrode obtained specific capacities of 371.9, 355.4, 340.4, 314.9, 255.2, and 158.8 mAh/g, respectively, while increasing current density from 1 to 20 A/g (Fig. 4D). By comparing the specific capacity at the initial stage of the reaction, the results show that the capacity retention is 68% when the current density is 10 A/g.

The superior electrochemical performance of the 2D-on-3D CoNi-LDHs NFs electrode can be attributed to several factors. Firstly, the ultrathin and two-dimensional architecture of the 2D-on-3D CoNi-LDHs NFs facilitated the charge transport, thereby enhancing the charge and discharge efficiency and capacity. Secondly, the 3D formation coupled with the ultrathin 2D nanosheets enables the influx of $OH^-$ anions into the nanoflowers, giving rise to the formation of CoOOH or NiOOH. Upon oxidation of $Co^{2+}$ and $Ni^{2+}$ ions in the 2D-on-3D CoNi-LDHs NFs, the average oxidation state escalates. To preserve electrical neutrality, more $OH^-$ anions permeate the nanoflowers. Lastly, the interleaved 2D-on-3D CoNi-LDHs NFs nanoflowers conjoin to produce a robust and durable 2D-on-3D CoNi-LDHs NFs configuration. This construction, replete with abundant mesoporous pores and defects, yields more active sites for the redox process and hastens ion diffusion, leading up to the exceptional electrochemical performance of the electrode. The long-term cycling

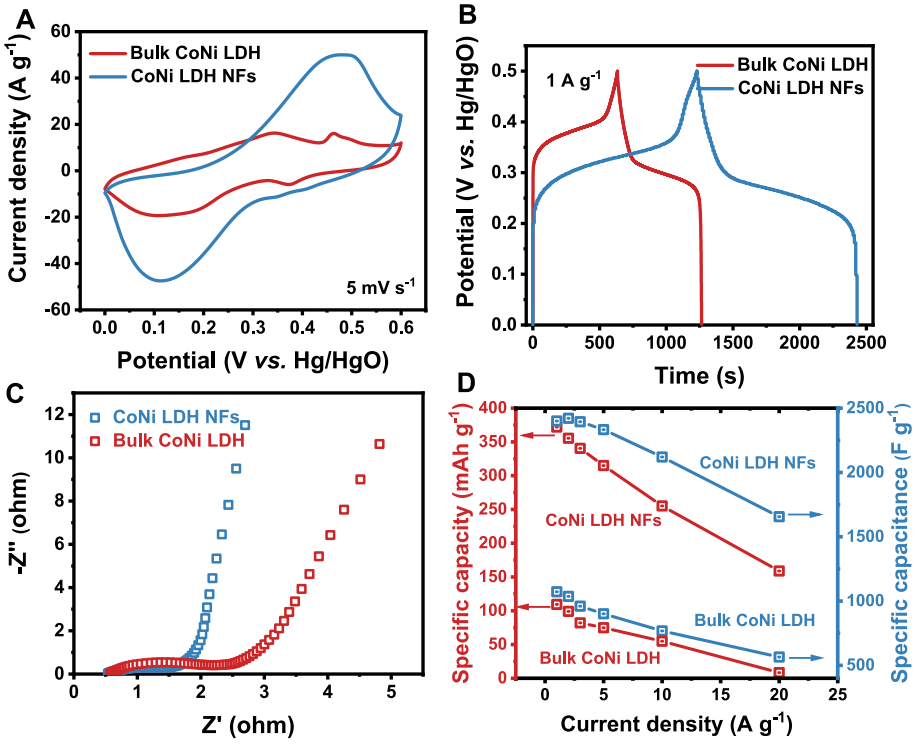


**Fig. 4.** Electrochemical performance of 2D-on-3D CoNi-LDH NFs and bulk CoNi-LDH NFs. **A** CV curves at 5 mV $s^{-1}$, **B** GCD curves at 1 A/g, **C** Nyquist curves, **D** Comparison curves of capacity and capacitance at 1 ~ 20 A/g.

stability of electrode materials is of crucial importance for practical energy storage devices. Therefore, cycling stability tests were performed at 5 A/g (Fig. S12). The 2D-on-3D CoNi-LDHs NFs electrode demonstrates outstanding stability, retaining 97.1% of its initial capacity after 2000 cycles.

In Fig. 5A and Fig. S13A, electrodes collected at different scan rates by 2D-on-3D CoNi-LDHs NFs usually present a pair of redox peaks between 0 and 0.6 V, and the well-defined redox peaks are mainly derived from Faradic redox reactions related to cobalt and nickel ions. By analyzing the intrinsic relationship between current ($i$) and sweep rate, the reaction kinetic characteristics ($v$) of 2D-on-3D CoNi-LDHs NFs electrode were evaluated according to the following equation:

$$i = av^b \tag{2}$$

where $a$ and $b$ are constants. In Fig. S13B, the $b$ values of the cathode and anode on the 2D-on-3D CoNi-LDHs NFs electrode are 0.63 and 0.60, respectively, indicating the dominant diffusion control battery-type process. The contribution of capacity and diffusion control to the total capacity can be described by the following equation:

$$i(V) = k_1 + k_2 v^{1/2} \tag{3}$$

where i(V) is the response current at a specific voltage, and $k_1 v$ and $k_2 v^{1/2}$ are the capacity contribution and diffusion control contribution, respectively. In Figs. S13C and S13D, when the scanning speed is 1, 2, 5, 8, and 10 mV $s^{-1}$, the contribution of diffusion control account for 58.2%, 63.5%, 71.1%, 75.3%, and 81.1% of the total capacity, respectively, indicating that the charge storage mechanism controlled by ion diffusion into the lattice. The greater contribution of diffusion control effect with increasing scanning rate is likely ascribed to the enhanced ion intercalation into the lattices.

To further evaluate its practical potential, an asymmetric supercapacitor (ASC, 2D-on-3D CoNi-LDHs NFs//N-rGO) was assembled using2D-on-3D CoNi-LDHs NFs as the positive electrode, N-rGO hydrogel as the negative electrode, and 3 M potassium hydroxide solution as the electrolyte. Fig. 5A shows CV curves of ASC in different potential windows at a scanning speed of 5 mV $s^{-1}$. Fig. 5B shows the CV diagram of 2D-on-3D CoNi-LDHs NFs//N-rGO ASC with different operating voltages from 1.2 to 1.7 V at a scanning rate of 5 mV $s^{-1}$, with a stable operating voltage up to 1.7 V without polarization. Fig. 5C shows the CV curves of 2D-on-3D CoNi-LDHs NFs//N-rGO ASC at scan speeds ranging from 5 to 100 mV $s^{-1}$ and potential windows of 0–1.7 V. The quasi-rectangular shape of the curve can be attributed to the good charge matching between the battery-type electrode and the electric bilayer material. Notably, the CV curves showed no significant deformation at all scan rates, exhibiting outstanding rate capability. The GCD curves of 2D-on-3D CoNi-LDHs NFs//N-rGO ASC are largely symmetric at current densities ranging from 1 to 10 A/g (Fig. 5D), implying its excellent electrochemical reversibility and superior coulomb efficiency. The specific capacity of 2D-on-3D CoNi-LDHs NFs//N-rGO ASC varies with current density (Fig. 5E). When the current density is 1 A/g, the specific capacity is 134.4 mAh/g. When the current density increased from 1.0 to 10 A/g, 55% of the capacity is retained. The specific capacity of 2D-on-3D CoNi-LDHs NFs//N-rGO ASC is much higher than that of CoNi-LDHs materials reported in recent studies (data listed in Table S3).

Based on the GCD curve, the energy and power density of 2D-on-3D CoNi-LDHs NFs//N-rGO ASC are given in the Ragone plot (Fig. 5F and Table S4). At a power density of 1.79 kW $kg^{-1}$, the energy density of the ASC device is 71.9 Wh $kg^{-1}$, and at a power density of 7.85 kW $kg^{-1}$, the energy density of the ASC device is 41.4 Wh $kg^{-1}$. The energy density of 2D-on-3D CoNi-LDHs NFs//N-rGO ASC is higher than that of recently reported cobalt–nickel-based hydroxides [29–30,44–58]. The ASC device exhibits excellent cycle stability (Fig. S14 and Table S3). After 5000 cycles with a current density of 10 A/g, 91.3% capacity of the ASC device was maintained, indicative of the good electrochemical performance of 2D-on-3D-CoNi-LDHs NFs//N-rGO ASC device. Moreover, the morphology of the 2D-on-3D CoNi LDH NFs//N-rGO was only slightly changed after 5000 cycles (Fig. S15). Taken together, these results demonstrate the promise and potential of 2D-on-3D CoNi LDH NFs in energy storage applications.

## 3. Conclusions

In conclusion, we have developed a method for the directed self-

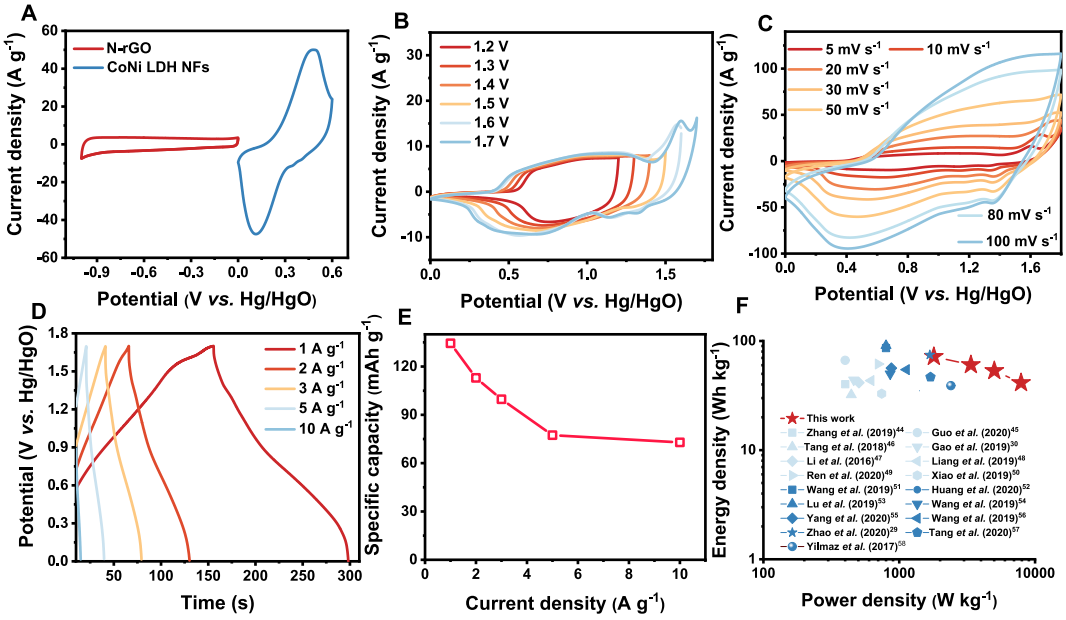


**Fig. 5.** Electrochemical performance of the 2D-on-3D CoNi-LDH NFs//N-rGO ASC. **A** CV curves of 2D-on-3D CoNi-LDH NFs and N-rGO obtained at a scan rate of 5 mV $s^{-1}$, **B** CV curves of 2D-on-3D CoNi-LDH NFs//N-rGO ASC in 3.0 M KOH with different operating voltages from 1.2 to 1.7 V at a scanning rate of 5 mV $s^{-1}$, **C** CV curves of 2D-on-3D CoNi-LDH NFs//N-rGO ASC at scan rates ranging from 5 to 100 mV $s^{-1}$ under 1.7 V voltage windows in 3.0 M KOH, **D** The GCD profiles of 2D-on-3D CoNi-LDH NFs//N-rGO ASC at current density from 1 to 10 A $g^{-1}$ under 1.7 V voltage window, **E** The capacity under different current density, **F** Energy and power densities of the 2D-on-3D CoNi-LDH NFs//N-rGO ASC compared with other supercapacitors.

assembly of 2D-on-3D CoNi-LDHs NFs into flower-shaped structures with nanopores-nanosheets. The process of directed self-assembly, characterized by oriented attachment and Ostwald ripening, facilitated controlled nucleation growth leading to the formation of the ultrathin 2D-on-3D CoNi-LDHs NFs. Using the synergistic effects of the ultrathin 2D-on-3D architecture, the optimized CoNi-LDHs NFs exhibited a remarkable specific capacity of 371 mAh/g (2400F/g) at a current density of 1.0 A/g. The asymmetric supercapacitor demonstrated an impressive energy density of 98.9 Wh $kg^{-1}$ at a high power density of 17981 W $kg^{-1}$ and demonstrated exceptional cycling stability, maintaining 91.3% capacity after 5000 cycles at 10.0 A/g. Our work presents a straightforward approach to the design and synthesis of novel ultrathin 2D-on-3D architecture nanomaterials for energy storage applications, and more importantly, reveals the mechanisms underlying the orientated self-assembly of these ultrathin 2D-on-3D architectures.

## 4. Experimental details

**Chemicals reagents.** Cobalt chloride hexahydrate, nickel chloride hexahydrate, and ethanolamine were purchased from Sigma-Aldrich. Sodium hydroxide and ethanol were received from Sinopharm Chemical Reagent. All the chemical reagents were used without further purification.

**Synthesis of 2D-on-3D CoNi-LDHs NFs.** Nickel chloride hexahydrate (0.02 mol) and cobalt chloride hexahydrate (0.02 mol) were dissolved in 125 mL of ethanol and deionized (DI) water (v/v = 1/4) with vigorously stirred for 10 min to form a homogeneous solution. Ethanolamine (5 mL) was dissolved in 60 mL of DI water/ethanol (v/v = 1/2). Then, the ethanolamine mixture solution was added dropwise into the homogeneous solution under vigorous stirring at 25 °C for 6 h. The resulting solid materials were washed with DI water and ethanol three times, and dried at 60 °C for 12 h.

**Synthesis of bulk CoNi LDH.** Nickel chloride hexahydrate (0.02 M) and cobalt chloride hexahydrate (0.02 M) were dissolved in 125 mL of ethanol and DI water (v/v = 1/4) with vigorously stirred for 10 min to form a homogeneous solution. Sodium hydroxide (0.04 M) was dissolved in 50 mL of DI water and ethanol (v/v = 1/2). Then, NaOH solution was added dropwise into the mixed solution under vigorous stirring at 25 °C for 6 h. Further, the resulting solid materials were washed with DI water and ethanol three times, and dried at 60 °C for 12 h.

**Synthesis of N-Doped rGO hydrogel.** The GO was synthesized by Hummer's method·$NH_3$·$H_2O$ (1 mL) was added dropwise into GO aqueous solution (10 mL, 2 mg $mL^{-1}$) and ultrasonicated for 1 h. The mixed suspension solution was shifted into a Teflon-lined stainless steel autoclave reaction at 120 °C for 12 h. After cooling to room temperature, the formed hydrogel materials were soaked repeatedly with DI water to remove impurities.

**Material characterization.** Scanning electron microscope (SEM) and energy dispersive spectroscopy (EDS) images were obtained with a field emission JEOL-7100F microscope. TEM and HRTEM images were collected with STEM/EDS microscopy (JEM-2100F, JEOL). Atomic force microscope (AFM) images were collected with a MultiMode V system. The crystallographic characterization of the as-synthesized materials was obtained using a Bruker D8 Advance X-ray diffractometer (XRD) with a Cu Ka X-ray source. X-ray photoelectron spectroscopy (XPS) was used for characterizing the electronic architectures of the materials (Thermo ESCALAB 250Xi). Electron paramagnetic resonance (EPR) spectroscopy measurements were performed on a model spectrometer operating at the X-band frequency (JES-FA200, JEOL). Nitrogen adsorption isotherms were carried out at 77 K on a surface area and porosity analyzer (ASAP 2020, Micrometrics). The samples were degassed in a vacuum at 150 °C for 8 h prior to the isotherm measurements.

***In situ* SAXS characterization.** *In situ* SAXS experiments were conducted at the BL16B1 beamline at the Advanced Photon Source of the Shanghai Synchrotron Radiation Facility with 20 keV X-ray energy. The exposure time is 1 s. The monomer, solvent, and precipitant were readily added in a sealed quartz tube and reacted at 25 °C. The data were collected from 7 spots on the quartz tube (1 s for each spot) to avoid beam damage. Reduction into scattering intensity profiles as a function of the scattering vector, $q$, was completed using a customized code at the beamline. Fitting was conducted with the Modeling tool of Irena to reveal the particle size.

**Electrochemical measurements.** The working electrodes were prepared using the 2D-on-3D CoNi-LDHs NFs active materials, acetylene black, and polytetrafluoroethylene (PTFE) with a mass ratio of 80:15:5 and mixed in ethanol to form a homogeneous slurry. The obtained electrode material was then vacuum-dried overnight at 120 °C. The active material loading was about 2.0 mg $cm^{-2}$. A Pt foil (10 mm × 10 mm) and Hg/HgO electrode were used as a counter and reference electrode, and 3 M KOH aqueous solution as the electrolyte. Cyclic voltammetry (CV), galvanostatic charge/discharge (GCD), and electrochemical impedance spectroscopy (EIS) tests were conducted on an electrochemical workstation (Chenhua 760).

The capacity $C_s$ (mAh/g) and mass-specific capacitance $C_m$ (F/g) in a galvanostatic charge − discharge can be evaluated according to:

$$C_s = \frac{2i\int Vdt}{m\Delta V} \tag{4}$$

$$C_m = \frac{i\Delta t}{m\Delta V} \tag{5}$$

where $i$ (mA) is the discharge current, $m$ (mg) is the mass of active material, $t$ (s) is the discharge time, $\Delta V$ (V) is the potential window, and $\int Vdt$ corresponds to the integral area of the discharge process.

**Asymmetric device assembly.** The asymmetric device was constructed with the 2D-on-3D CoNi-LDHs NFs as the positive electrode material, N-rGO as the negative electrode material. The asymmetric devices cycling stability was tested on a Land CT2001A battery testing system. The mass ratio of the two electrodes is determined according to the charge balance equation:

$$\frac{m^+}{m^-} = \frac{C^- V^-}{C^+ V^+} \tag{6}$$

where $m^+$ and $m^-$ are the loading mass of the 2D-on-3D CoNi-LDHs NFs and N-rGO, $C^+$ and $C^-$ are the specific capacity of 2D-on-3D CoNi-LDHs NFs and N-rGO electrodes, $V^+$ and $V^-$ are the voltage range of one scanning segment of 2D-on-3D CoNi-LDHs NFs and N-rGO electrodes, respectively. The gravimetric energy density ($E_m$, Wh $kg^{-1}$) and power density ($P_m$, W $kg^{-1}$) of the cell can be estimated according to the following equations:

$$E_m = \frac{C_m V^2}{2} \tag{7}$$

$$P_m = \frac{E_m}{t} \tag{8}$$

where $C_m$ is the cell capacitance, $V$ refers to the operation potential window, and $t$ is the discharge time.

## CRediT authorship contribution statement

**Jingjing Cao:** Validation, Formal analysis. **Zimou Feng:** Validation, Formal analysis. **Huaxing Liang:** Investigation, Methodology. **Xinglin Lu:** Supervision, Writing – review & editing, Funding acquisition, Project administration. **Wei Wang:** Supervision, Writing – review & editing.

## Declaration of Competing Interest

The authors declare that they have no known competing financial

interests or personal relationships that could have appeared to influence the work reported in this paper.

## Data availability

No data was used for the research described in the article.

## Acknowledgment

We acknowledge the partial financial support received from the National Science Foundation of China (Award No. 52170094) and the Fundamental Research Funds for the Central Universities. SAXS characterization performed on beamline BL16B1 at the Shanghai Synchrotron Radiation Facility was assisted by Dr. Xiaran Miu and Dr. Feng Tian under the proposal 2022-SSRF-PT-020452. This work was partially carried out at the USTC Center for Micro- and Nanoscale Research and Fabrication.

## Appendix A. Supplementary data

Supplementary data to this article can be found online at https://doi.org/10.1016/j.cej.2023.144872.

## References

[1] M. Shao, R. Zhang, Z. Li, M. Wei, D.G. Evans, X. Duan, Layered double hydroxides toward electrochemical energy storage and conversion: design, synthesis and applications, Chem. Commun. (Camb) 51 (88) (2015) 15880–15893.
[2] P.J. Sideris, U.G. Nielsen, Z. Gan, C.P. Grey, Mg/Al ordering in layered double hydroxides revealed by multinuclear NMR spectroscopy, Science 321 (2008) 113–117.
[3] D. Zhou, P. Li, X. Lin, A. McKinley, Y. Kuang, W. Liu, W.F. Lin, X. Sun, X. Duan, Layered double hydroxide-based electrocatalysts for the oxygen evolution reaction: identification and tailoring of active sites, and superaerophobic nanoarray electrode assembly, Chem. Soc. Rev. 50 (2021) 8790–8817.
[4] Q. Wang, D. O'Hare, Recent advances in the synthesis and application of layered double hydroxide (LDH) nanosheets, Chem. Rev. 112 (2012) 4124–4155.
[5] G. Sun, L. Sun, H. Wen, Z. Jia, K. Huang, C. Hu, From Layered Double Hydroxide to Spinel Nanostructures: Facile Synthesis and Characterization of Nanoplatelets and Nanorods, J. Phys. Chem. B 110 (2006) 13375–13380.
[6] S. Zhao, Q. Liang, W. Gao, M. Zhou, C. Yao, S. Xu, Z. Li, In Situ Growth of ZnIn2S4 on MOF-Derived Ni–Fe LDH to Construct Ternary-Shelled Nanotubes for Efficient Photocatalytic Hydrogen Evolution, Inorg. Chem. 60 (2021) 9762–9772.
[7] W. Lv, Q. Mei, M. Du, J. Xiao, W. Ye, Q. Zheng, Interaction between Poly(vinyl alcohol) and Layered Double Hydroxide (LDH) Particles with Different Topological Shape and Their Application in Electrospinning, J. Phys. Chem. C 120 (2016) 14435–14443.
[8] D. Yang, R. Wang, J. Zhang, Z. Liu, Synthesis of Nickel Hydroxide Nanoribbons with a New Phase: A Solution Chemistry Approach, J. Phys. Chem. B 108 (2004) 7531–7533.
[9] J. Cao, Q. Mei, R. Wu, W. Wang, Flower-like nickel–cobalt layered hydroxide nanostructures for super long-life asymmetrical supercapacitors, Electrochim. Acta 321 (2019), 134711.
[10] J. Cao, T. Zhou, Y. Xu, Y. Qi, W. Jiang, W. Wang, P. Sun, A. Li, Q. Zhang, Oriented Assembly of Anisotropic Nanosheets into Ultrathin Flowerlike Superstructures for Energy Storage, ACS Nano 15 (2021) 2707–2718.
[11] J. Liang, R. Ma, N. Iyi, Y. Ebina, K. Takada, T. Sasaki, Topochemical Synthesis, Anion Exchange, and Exfoliation of Co−Ni Layered Double Hydroxides: A Route to Positively Charged Co−Ni Hydroxide Nanosheets with Tunable Composition, Chem. Mater. 22 (2009) 371–378.
[12] N. Kim, T.H. Gu, D. Shin, X. Jin, H. Shin, M.G. Kim, H. Kim, S.J. Hwang, Lattice Engineering to Simultaneously Control the Defect/Stacking Structures of Layered Double Hydroxide Nanosheets to Optimize Their Energy Functionalities, ACS Nano 15 (2021) 8306–8318.
[13] L. Hui, Y. Xue, B. Huang, H. Yu, C. Zhang, D. Zhang, D. Jia, Y. Zhao, Y. Li, H. Liu, Y. Li, Overall water splitting by graphdiyne-exfoliated and -sandwiched layered double-hydroxide nanosheet arrays, Nat. Commun. 9 (2018) 5309.
[14] P. Zhai, M. Xia, Y. Wu, G. Zhang, J. Gao, B. Zhang, S. Cao, Y. Zhang, Z. Li, Z. Fan, C. Wang, X. Zhang, J.T. Miller, L. Sun, J. Hou, Engineering single-atomic ruthenium catalytic sites on defective nickel-iron layered double hydroxide for overall water splitting, Nat. Commun. 12 (2021) 4587.
[15] K. Fan, H. Chen, Y. Ji, H. Huang, P.M. Claesson, Q. Daniel, B. Philippe, H. Rensmo, F. Li, Y. Luo, L. Sun, Nickel-vanadium monolayer double hydroxide for efficient electrochemical water oxidation, Nat. Commun. 7 (2016) 11981.
[16] J.L. Gunjakar, T.W. Kim, H.N. Kim, I.Y. Kim, S.-J. Hwang, Mesoporous Layer-by-Layer Ordered Nanohybrids of Layered Double Hydroxide and Layered Metal Oxide: Highly Active Visible Light Photocatalysts with Improved Chemical Stability, J. Am. Chem. Soc. 133 (2011) 14998–15007.
[17] H. Li, H. Zhu, Y. Shi, H. Shang, L. Zhang, J. Wang, Vacancy-Rich and Porous NiFe-Layered Double Hydroxide Ultrathin Nanosheets for Efficient Photocatalytic NO Oxidation and Storage, Environ. Sci. Tech. 56 (2022) 1771–1779.
[18] P. Li, M. Wang, X. Duan, L. Zheng, X. Cheng, Y. Zhang, Y. Kuang, Y. Li, Q. Ma, Z. Feng, W. Liu, X. Sun, Boosting oxygen evolution of single-atomic ruthenium through electronic coupling with cobalt-iron layered double hydroxides, Nat. Commun. 10 (2019) 1711.
[19] H. Liang, F. Meng, M. Cabán-Acevedo, L. Li, A. Forticaux, L. Xiu, Z. Wang, S. Jin, Hydrothermal Continuous Flow Synthesis and Exfoliation of NiCo Layered Double Hydroxide Nanosheets for Enhanced Oxygen Evolution Catalysis, Nano Lett. 15 (2015) 1421–1427.
[20] J.T. Mefford, A.R. Akbashev, M. Kang, C.L. Bentley, W.E. Gent, H.D. Deng, D. H. Alsem, Y.S. Yu, N.J. Salmon, D.A. Shapiro, P.R. Unwin, W.C. Chueh, Correlative operando microscopy of oxygen evolution electrocatalysts, Nature 593 (2021) 67–73.
[21] F. Song, X. Hu, Exfoliation of layered double hydroxides for enhanced oxygen evolution catalysis, Nat. Commun. 5 (2014) 4477.
[22] Z. Hao, X. He, H. Li, D. Trefilov, Y. Song, Y. Li, X. Fu, Y. Cui, S. Tang, H. Ge, Y. Chen, Vertically Aligned and Ordered Arrays of 2D $MCo_2S_4$@Metal with Ultrafast Ion/Electron Transport for Thickness-Independent Pseudocapacitive Energy Storage, ACS Nano 14 (10) (2020) 12719–12731.
[23] Z.-H. Huang, F.-F. Sun, M. Batmunkh, W.-H. Li, H. Li, Y. Sun, Q. Zhao, X. Liu, T.-Y. Ma, Zinc–nickel–cobalt ternary hydroxide nanoarrays for high-performance supercapacitors, J. Mater. Chem. A 7 (19) (2019) 11826–11835.
[24] R. Liu, A.o. Zhou, X. Zhang, J. Mu, H. Che, Y. Wang, T.-T. Wang, Z. Zhang, Z. Kou, Fundamentals, advances and challenges of transition metal compounds-based supercapacitors, Chem. Eng. J. 412 (2021) 128611.
[25] S.A. Chala, M.-C. Tsai, W.-N. Su, K.B. Ibrahim, B. Thirumalraj, T.-S. Chan, J.-F. Lee, H. Dai, B.-J. Hwang, Hierarchical 3D Architectured Ag Nanowires Shelled with NiMn-Layered Double Hydroxide as an Efficient Bifunctional Oxygen Electrocatalyst, ACS Nano 14 (2) (2020) 1770–1782.
[26] Y. Hou, Z. Wen, S. Cui, X. Feng, J. Chen, Strongly Coupled Ternary Hybrid Aerogels of N-deficient Porous Graphitic-$C_3N_4$ Nanosheets/N-Doped Graphene/NiFe-Layered Double Hydroxide for Solar-Driven Photoelectrochemical Water Oxidation, Nano Lett. 16 (2016) 2268–2277.
[27] P.C. Lohani, A.P. Tiwari, K. Chhetri, A. Muthurasu, B. Dahal, S.-H. Chae, T.H. Ko, J. Y. Lee, Y.S. Chung, H.Y. Kim, Polypyrrole Nanotunnels with Luminal and Abluminal Layered Double Hydroxide Nanosheets Grown on a Carbon Cloth for Energy Storage Applications, ACS Appl. Mater. Interfaces 14 (2022) 23285–23296.
[28] F. Grote, Z.-Y. Yu, J.-L. Wang, S.-H. Yu, Y. Lei, Self-Stacked Reduced Graphene Oxide Nanosheets Coated with Cobalt-Nickel Hydroxide by One-Step Electrochemical Deposition toward Flexible Electrochromic Supercapacitors, Small 11 (2015) 4666–4672.
[29] Y. Guo, X. Hong, Y. Wang, Q. Li, J. Meng, R. Dai, X. Liu, L. He, L. Mai, Multicomponent Hierarchical Cu-Doped NiCo-LDH/CuO Double Arrays for Ultralong-Life Hybrid Fiber Supercapacitor, Adv. Funct. Mater. 29 (2019) 1809004.
[30] X. Gao, X. Liu, D. Wu, B. Qian, Z. Kou, Z. Pan, Y. Pang, L. Miao, J. Wang, Significant Role of Al in Ternary Layered Double Hydroxides for Enhancing Electrochemical Performance of Flexible Asymmetric Supercapacitor, Adv. Funct. Mater. 29 (2019) 1903879.
[31] J. Balamurugan, T.T. Nguyen, V. Aravindan, N.H. Kim, J.H. Lee, Flexible Solid-State Asymmetric Supercapacitors Based on Nitrogen-Doped Graphene Encapsulated Ternary Metal-Nitrides with Ultralong Cycle Life, Adv. Funct. Mater. 28 (2018) 1804663.
[32] L. Lv, Z. Yang, K. Chen, C. Wang, Y. Xiong, 2D Layered Double Hydroxides for Oxygen Evolution Reaction: From Fundamental Design to Application, Adv. Energy Mater. 9 (2019) 1803358.
[33] H. Yi, S. Liu, C. Lai, G. Zeng, M. Li, X. Liu, B. Li, X. Huo, L. Qin, L. Li, M. Zhang, Y. Fu, Z. An, L. Chen, Recent Advance of Transition-Metal-Based Layered Double Hydroxide Nanosheets: Synthesis, Properties, Modification, and Electrocatalytic Applications, Adv. Energy Mater. 11 (2021) 2002863.
[34] G. Hu, D. O'Hare, Unique Layered Double Hydroxide Morphologies Using Reverse Microemulsion Synthesis, J. Am. Chem. Soc. 127 (2005) 17808–17813.
[35] S. Ma, L. Huang, L. Ma, Y. Shim, S.M. Islam, P. Wang, L.-D. Zhao, S. Wang, G. Sun, X. Yang, M.G. Kanatzidis, Efficient Uranium Capture by Polysulfide/Layered Double Hydroxide Composites, J. Am. Chem. Soc. 137 (2015) 3670–3677.
[36] Z.P. Xu, G.S. Stevenson, C.-Q. Lu, G.Q. Lu, P.F. Bartlett, P.P. Gray, Stable Suspension of Layered Double Hydroxide Nanoparticles in Aqueous Solution, J. Am. Chem. Soc. 128 (2006) 36–37.
[37] Z. Liu, R. Ma, M. Osada, N. Iyi, Y. Ebina, K. Takada, T. Sasaki, Synthesis, Anion Exchange, and Delamination of Co−Al Layered Double Hydroxide: Assembly of the Exfoliated Nanosheet/Polyanion Composite Films and Magneto-Optical Studies, J. Am. Chem. Soc. 128 (2006) 4872–4880.
[38] T. Sudare, T. Yamaguchi, M. Ueda, H. Shiiba, H. Tanaka, M. Tipplook, F. Hayashi, K. Teshima, Critical role of water structure around interlayer ions for ion storage in layered double hydroxides, Nat. Commun. 13 (2022) 6448.
[39] L. Wan, M. Pang, J. Le, Z. Xu, H. Zhou, Q. Xu, B. Wang, Oriented intergrowth of the catalyst layer in membrane electrode assembly for alkaline water electrolysis, Nat. Commun. 13 (2022).
[40] S. Liu, M. Dong, Y. Wu, S. Luan, Y. Xin, J. Du, S. Li, H. Liu, B. Han, Solid surface frustrated Lewis pair constructed on layered AlOOH for hydrogenation reaction, Nat. Commun. 13 (2022) 2320.
[41] D. Wang, Q. Li, C. Han, Q. Lu, Z. Xing, X. Yang, Atomic and electronic modulation of self-supported nickel-vanadium layered double hydroxide to accelerate water splitting kinetics, Nat. Commun. 10 (2019) 3899.

[42] Y. Bai, Y. Wu, X. Zhou, Y. Ye, K. Nie, J. Wang, M. Xie, Z. Zhang, Z. Liu, T. Cheng, C. Gao, Promoting nickel oxidation state transitions in single-layer NiFeB hydroxide nanosheets for efficient oxygen evolution, Nat. Commun. 13 (2022) 6094.
[43] H. You, D. Wu, D. Si, M. Cao, F. Sun, H. Zhang, H. Wang, T.-F. Liu, R. Cao, Monolayer NiIr-Layered Double Hydroxide as a Long-Lived Efficient Oxygen Evolution Catalyst for Seawater Splitting, J. Am. Chem. Soc. 144 (2022) 9254–9263.
[44] H. Zhang, B. Xu, H. Mei, Y. Mei, S. Zhang, Z. Yang, Z. Xiao, W. Kang, D. Sun, "HOT" Alkaline Hydrolysis of Amorphous MOF Microspheres to Produce Ultrastable Bimetal Hydroxide Electrode with Boosted Cycling Stability, Small 15 (49) (2019) e1904663.
[45] W. Guo, C. Dun, C. Yu, X. Song, F. Yang, W. Kuang, Y. Xie, S. Li, Z. Wang, J. Yu, G. Fu, J. Guo, M.A. Marcus, J.J. Urban, Q. Zhang, J. Qiu, Mismatching integration-enabled strains and defects engineering in LDH microstructure for high-rate and long-life charge storage, Nat. Commun. 13 (2022) 1409.
[46] X. Tang, C. Zhu, D. Cheng, H. Zhou, X. Liu, P. Xie, Q. Zhao, D.i. Zhang, T. Fan, Architectured Leaf-Inspired $Ni_{0.33}Co_{0.66}S_2$/Graphene Aerogels via 3D Printing for High-Performance Energy Storage, Adv. Funct. Mater. 28 (51) (2018) 1805057.
[47] X. Li, L.e. Wang, J. Shi, N. Du, G. He, Multishelled Nickel-Cobalt Oxide Hollow Microspheres with Optimized Compositions and Shell Porosity for High-Performance Pseudocapacitors, ACS Appl. Mater. Interfaces 8 (27) (2016) 17276–17283.
[48] Z. Liang, C. Qu, W. Zhou, R. Zhao, H. Zhang, B. Zhu, W. Guo, W. Meng, Y. Wu, W. Aftab, Q. Wang, R. Zou, Synergistic Effect of Co–Ni Hybrid Phosphide Nanocages for Ultrahigh Capacity Fast Energy Storage, Adv. Sci. 6 (8) (2019) 1802005.
[49] C. Ren, X.u. Jia, W. Zhang, D. Hou, Z. Xia, D. Huang, J. Hu, S. Chen, S. Gao, Hierarchical Porous Integrated $Co_{1-x}S/CoFe_2O_4$@rGO Nanoflowers Fabricated via Temperature-Controlled In Situ Calcining Sulfurization of Multivariate CoFe-MOF-74@rGO for High-Performance Supercapacitor, Adv. Funct. Mater. 30 (45) (2020) 2004519.
[50] Z. Xiao, Y. Mei, S. Yuan, H. Mei, B. Xu, Y. Bao, L. Fan, W. Kang, F. Dai, R. Wang, L. Wang, S. Hu, D. Sun, H.-C. Zhou, Controlled Hydrolysis of Metal-Organic Frameworks: Hierarchical Ni/Co-Layered Double Hydroxide Microspheres for High-Performance Supercapacitors, ACS Nano 13 (6) (2019) 7024–7030.
[51] W. Wang, Y. Lu, M. Zhao, R. Luo, Y. Yang, T. Peng, H. Yan, X. Liu, Y. Luo, Controllable Tuning of Cobalt Nickel-Layered Double Hydroxide Arrays as Multifunctional Electrodes for Flexible Supercapattery Device and Oxygen Evolution Reaction, ACS Nano 13 (2019) 12206–12218.
[52] J. Huang, Y. Xiong, Z. Peng, L. Chen, L. Wang, Y. Xu, L. Tan, K. Yuan, Y. Chen, A General Electrodeposition Strategy for Fabricating Ultrathin Nickel Cobalt Phosphate Nanosheets with Ultrahigh Capacity and Rate Performance, ACS Nano 14 (2020) 14201–14211.
[53] W. Lu, J. Shen, P. Zhang, Y. Zhong, Y. Hu, X.W. Lou, Construction of CoO/Co-Cu-S Hierarchical Tubular Heterostructures for Hybrid Supercapacitors, Angew. Chem. Int. Ed. 58 (2019) 15441–15447.
[54] Q. Wang, Y. Luo, R. Hou, S. Zaman, K. Qi, H. Liu, H.S. Park, B.Y. Xia, Redox Tuning in Crystalline and Electronic Structure of Bimetal-Organic Frameworks Derived Cobalt/Nickel Boride/Sulfide for Boosted Faradaic Capacitance, Adv. Mater. 31 (51) (2019) e1905744.
[55] Q. Yang, Q. Wang, Y. Long, F. Wang, L. Wu, J. Pan, J. Han, Y. Lei, W. Shi, S. Song, In Situ Formation of $Co_9S_8$Quantum Dots in MOF-Derived Ternary Metal Layered Double Hydroxide Nanoarrays for High-Performance Hybrid Supercapacitors, Adv. Energy Mater. 10 (2020) 1903193.
[56] Y. Wang, H. Wei, H. Lv, Z. Chen, J. Zhang, X. Yan, L. Lee, Z.M. Wang, Y.-L. Chueh, Highly Stable Three-Dimensional Nickel-Cobalt Hydroxide Hierarchical Heterostructures Hybridized with Carbon Nanotubes for High-Performance Energy Storage Devices, ACS Nano 13 (2019) 11235–11248.
[57] Y. Tang, H. Shen, J. Cheng, Z. Liang, C. Qu, H. Tabassum, R. Zou, Fabrication of Oxygen-Vacancy Abundant NiMn-Layered Double Hydroxides for Ultrahigh Capacity Supercapacitors, Adv. Funct. Mater. 30 (2020) 1908223.
[58] G. Yilmaz, K.M. Yam, C. Zhang, H.J. Fan, G.W. Ho, In Situ Transformation of MOFs into Layered Double Hydroxide Embedded Metal Sulfides for Improved Electrocatalytic and Supercapacitive Performance, Adv. Mater. 29 (2017) 1606814.